symmetry

MDPI

Article

Effect of Ni Addition on the Phase Balance and Grain Boundary Character Distribution in 2507 Super Duplex Stainless Steel Fabricated via LPBF

Przemysław Snopiński [1,*], Beatrice Ardayfio [1], Mengistu Dagnaw [1], Mariusz Król [1], Michal Kotoul [2] and Zbigniew Brytan [1]

[1] Department of Engineering Materials and Biomaterials, Faculty of Mechanical Engineering, Silesian University of Technology, 44-100 Gliwice, Poland; mengistu.jemberu.dagnaw@polsl.pl (M.D.); zbigniew.brytan@polsl.pl (Z.B.)
[2] Institute of Solid Mechanics, Mechatronics and Biomechanics, Brno University of Technology, Technická 2896/2, 616 69 Brno, Czech Republic
* Correspondence: przemyslaw.snopinski@polsl.pl

Abstract

Super duplex stainless steels (SDSSs) can be effectively fabricated via Laser Powder Bed Fusion (LPBF), yet achieving the necessary phase balance remains a critical metallurgical challenge. The rapid solidification rates inherent to the LPBF process typically result in a predominantly ferritic microstructure. Since CSL boundaries—specifically high-symmetry ∑3 twins—form preferentially in the austenite phase, achieving a high fraction of these boundaries in the ferritic as-built LPBF state remains a significant challenge. To address this limitation, we implemented a feedstock modification strategy by mechanically blending 2507 SDSS powder with 3 and 6 wt.% elemental nickel prior to LPBF processing. The microstructural evolution, phase distribution, and boundary character were comprehensively evaluated using Electron Backscatter Diffraction (EBSD). Analysis revealed that the addition of nickel did not compromise densification, with all samples achieving relative densities exceeding 99.2%. While the base alloy remained 98.5% ferritic, the addition of 6 wt.% Ni successfully promoted the formation of approximately 31.1 wt.% austenite, characterized by intragranular laths formed via a massive-like transformation mechanism[6]. Crucially, despite the theoretical increase in Stacking Fault Energy (SFE) associated with high nickel content, the restored austenite phase exhibited a significant fraction of high-symmetry CSL ∑3 twin boundaries (rising to 7.05%). These findings demonstrate that compositional modification can overcome the kinetic limitations of the LPBF process, facilitating the development of a favorable Grain Boundary Character Distribution (GBCD).

Keywords: super duplex stainless steel; microstructure; grain boundary engineering; additive manufacturing

Academic Editors: André Barros, Noé Cheung, Felipe Bertelli and Vasilis K. Oikonomou

Received: 15 December 2025
Revised: 9 January 2026
Accepted: 16 January 2026
Published: 21 January 2026

1. Introduction

Duplex stainless steels (DSSs) are a critical class of advanced materials characterized by dual-phase microstructure, which consists of near-equal parts of austenite and ferrite [1,2]. This microstructure is the key to their favorable mechanical properties and superior corrosion resistance, making DSS essential for aggressive environments where they compete predominantly with higher alloy austenitic grades [3,4]. However, this austenite–ferrite

balance is highly sensitive to thermal processing [5]. Under non-equilibrium cooling conditions, the required phase balance is not maintained. This poses a significant challenge to fabricate dependable DSS components.

The challenge of maintaining phase balance is also well-documented in conventional manufacturing processes like welding. In this process, rapid cooling rates in the Heat-Affected Zone (HAZ) and weld metal kinetically favor ferrite formation and grain coarsening, often resulting in a predominantly ferritic structure [6–9]. This issue is even more pronounced in Additive Manufacturing (AM) processes such as LPBF. The extremely rapid solidification inherent to LPBF creates a kinetic barrier to austenite formation, consistently yielding components with critically low austenite fractions [10].

To address this, traditional strategies have relied on process control, post-process heat treatments, or compositional modification [11,12]. While post-process treatments like solution annealing can effectively restore phase equilibrium, they introduce significant cost and complexity. Consequently, there is a strong drive for metallurgical strategies that promote austenite formation directly during the manufacturing process. In welding, for instance, Baghdadchi et al. [7] demonstrated that substituting argon with nitrogen shielding gas effectively stabilizes austenite. A more robust approach, however, involves the intentional addition of nickel. As a potent austenite stabilizer, nickel counteracts the ferrite-promoting effects of rapid cooling and elements like chromium [11]. This efficacy is well-proven in welding applications; for example, da Cruz Junior utilized a 30 µm nickel foil to successfully balance austenite and ferrite fractions within the weld bead [13].

This principle is directly transferable and perhaps even more critical for AM DSS. The true potential of this approach lies in the unique capabilities of AM. The powder alloying allows for precise control over nickel concentrations within the melt pool. Previous studies confirm that increasing the nickel content correlates directly with increased austenite fraction, which is critical for applications requiring enhanced toughness. Furthermore, this in situ addition of nickel has been found to successfully promote austenite formation even at the high cooling rates characteristic of AM [14].

However, restoring the phase balance is not the sole requirement for microstructural optimization; the specific crystallographic symmetry of the grain boundaries is equally decisive. Recent research has increasingly focused on GBE, a processing strategy that aims to enhance bulk material properties by optimizing the GBCD through the manipulation of crystal lattice symmetry [15–18]. The central objective of GBE is to interrupt the connectivity of random High-Angle Grain Boundaries (HAGBs). From a crystallographic perspective, these random boundaries lack specific symmetry relationships, resulting in high interfacial energy and susceptibility to degradation. By introducing a high fraction of Coincidence Site Lattice (CSL) boundaries—specifically $\sum 3$ twins—the continuous network of random boundaries can be topologically disrupted [19,20]. These special interfaces are defined by precise rotational symmetry operations (e.g., a 60° rotation) around the <111> axis for $\sum 3$, which maximize atomic ordering and minimize free volume. When the fraction of these high-symmetry interfaces exceeds the certain threshold, the connectivity of the random boundary network is broken, significantly improving resistance to intergranular corrosion and stress corrosion cracking [21,22]. Thus, for super duplex stainless steels, the ability to engineer these symmetry-related interfaces offers a pathway to durability that extends beyond simple phase fraction control [23].

The formation of $\sum 3$ twins is intrinsic to the face-centered cubic (FCC) austenite phase and is fundamentally governed by the material's Stacking Fault Energy (SFE). In low-SFE materials, perfect dislocations readily dissociate into Shockley partial dislocations [24], creating a stacking fault ribbon that serves as a nucleus for twin formation during recrystallization. Conversely, increasing the SFE of the alloy restricts dissociation, promoting

dislocation cross-slip instead of twinning. This creates a theoretical conflict for 2507 SDSS: while nickel is the essential element to restore the austenite phase [25], thermodynamic calculations based on Schramm and Reed [26] indicate that adding 6 wt.% Ni raises the SFE of the austenite from approximately 50.0 mJ/m^2 to 87.2 mJ/m^2. Theoretically, this increase would suppress the atomistic mechanisms required to form twin boundaries. In this system, however, the principal limitation to GBE is not the SFE, but the scarcity of the austenite phase itself. The as-built LPBF microstructure is composed predominantly of a body-centered cubic (BCC) δ-ferrite matrix. Consequently, the austenite-stabilizing effect of nickel serves to restore the necessary phase balance, allowing the solid-state transformation to proceed via specific orientation relationships (e.g., Kurdjumov–Sachs). These crystallographic ORs are energetically favorable for the development of coherent, low-energy interfaces, which effectively compensate for the kinetic disadvantages imposed by the elevated SFE and high cooling rates of LPBF.

The objective of the present study is to demonstrate that the modification of SDSS 2507 with nickel promotes the formation of a critical volume fraction of austenite during non-equilibrium cooling, thereby establishing the microstructural prerequisites necessary for GBE in additively manufactured SDSS components.

2. Materials and Methods

2.1. Feedstock and Powder Preparation

The base material utilized for this investigation was gas-atomized super duplex stainless steel (SDSS) powder, grade UNS S32750 (EN 1.4410). The commercial powder is characterized by a spherical morphology with a particle size distribution ranging from 15 to 53 μm, ensuring high flowability for additive manufacturing processes. The nominal chemical composition of the base 2507 powder is provided in Table 1.

Table 1. Nominal chemical composition of the base 2507 powder.

Element	Fe	Cr	Ni	Mo	Mn	Si	Cu	N	C	O	P
wt.%	Bal	25	6.3	3.8	0.4	0.3	0.15	0.3	0.02	0.02	0.02

To investigate the influence of nickel content on the alloy's performance, three distinct feedstock batches were prepared via mechanical alloying:

1. Sample A (Base): pure 2507 SDSS powder.
2. Sample B (+3% Ni): 2507 SDSS powder blended with 3 wt.% elemental nickel powder.
3. Sample C (+6% Ni): 2507 SDSS powder blended with 6 wt.% elemental nickel powder.

The calculated chemical composition is given in Table 2.

Table 2. Chemical composition of the modified 2507 powders.

Element	Fe	Cr	Ni	Mo	Mn	Si	Cu	N	C	O	P
3% Ni over-alloyed sample, wt.%	Bal	24.25	9.1	3.69	0.39	0.34	0.15	0.29	0.02	0.016	0.02
6% Ni over-alloyed sample, wt.%	Bal	23.50	11.9	3.57	0.38	0.33	0.14	0.28	0.01	0.02	0.02

All powder compositions were precisely weighed to the required wt.% using a high-precision analytical balance. The blending process was performed in a turbula shaker mixer. To ensure a completely randomized solid–solid mixture and mitigate particle segregation (a risk due to differences in density and particle size between the SDSS and elemental Ni powders), the powders were mixed at a controlled rotational speed for 20 min.

2.2. LPBF Process

The LPBF process was conducted using a Renishaw AM125 (Renishaw, Wotton-under-Edge, UK) system. This machine utilizes an ytterbium (Yb) fiber laser with a wavelength of 1074 nm and a maximum power output of 200 W. The build chamber was maintained under a high-purity Argon atmosphere (oxygen content < 10 ppm) to prevent oxidation during the LPBF process. The components were fabricated on mild steel platforms.

A meander scanning strategy incorporating a 67° rotation between successive layers was utilized to mitigate residual stress and microstructural anisotropy. To ensure experimental consistency, all three feedstock variations were processed using identical parameters, previously optimized to maximize densification and minimize defect formation in 2507 SDSS (Sandvik Osprey Ltd., Neath, UK). This approach allowed the influence of nickel modification to be isolated from processing-induced variability. The specific LPBF process parameters are given in Table 3.

Table 3. LPBF process parameters used for fabrication 2507 super duplex stainless-steel samples.

Laser power (P)	180 W
Scanning speed (v)	300 mm/s
Hatch distance (h)	120 μm
Layer thickness (t)	30 μm
Volumetric energy density	166 J/mm^3

While direct EDS analysis was not performed on the loose powder mixtures prior to processing, the homogeneity of the elemental Ni distribution was ensured through the rigorous mechanical blending protocol described in Section 2.1. The efficacy of this mixing strategy was subsequently verified by the microstructural consistency of the final LPBF-fabricated parts. To further confirm the uniformity of element distribution within the solidified matrix, Energy-Dispersive Spectroscopy (EDS) analysis was performed on the as-built samples. The resulting elemental maps and point analysis data, provided in the Supplementary Materials (Figures S2 and S3), demonstrate a homogeneous distribution of nickel and other alloying elements within the sample over-alloyed with 6 wt.% Ni, confirming that the applied mixing parameters successfully mitigated particle segregation during the layer-by-layer fabrication process.

2.3. Microstructural Characterization

Following the LPBF process, the samples were removed from the build plate and prepared for metallographic examination. The specimens were mechanically ground and polished using a Struers automatic polishing device (Struers, Copenhagen, Denmark). The grinding process utilized a distinct sequence of silicon carbide (SiC) abrasive papers ranging from 500 to 1200 grit. Subsequently, the samples were subjected to fine-cloth polishing using diamond suspensions of 6, 3, and 1 μm, followed by a final polish with a 0.04 μm colloidal silica suspension for 30 min to obtain a mirror-like surface suitable for light optical and electron microscopy.

Initial microstructural observations were conducted in bright-field mode using a Zeiss Axio Observer Z1 inverted light optical microscope (Carl Zeiss, Jena, Germany). To reveal

the dual-phase microstructure and grain boundaries, chemical etching was performed using a Kalling No. 2 etchant with the following chemical composition: 5 g $CuCl_2$ + 100 mL HCl + 100 mL ethanol. To reveal microstructural constituents, mirror-like polished samples were immersed in an etchant for 3 min.

Crystallographic orientation mappings were performed via EBSD. Data acquisition was conducted using a Zeiss SUPRA 25 Field Emission Scanning Electron Microscope (FE-SEM) equipped with EDAX NT EBSD detector using a step size of 0.8 µm.

Prior to quantitative analysis, acquired raw EBSD data were subjected to a standard cleanup procedure to minimize noise and improve indexing reliability using TSL OIM software. The clean-up procedure utilized neighbor orientation correlation and neighbor Confidence Index (CI) correlation algorithms. To ensure data integrity, a minimum Confidence Index (CI) of 0.1 was applied. For grain reconstruction, a grain tolerance angle of 5° was defined, and a minimum grain size of 9 pixels was set to exclude artifacts.

CSL boundary analysis was based on the Brandon criterion with a fixed angular tolerance of 5°. A boundary was classified as CSL if its misorientation angle fell within 5°of a theoretical CSL misorientation (ΘCSL), meaning $|\Delta\Theta\text{-}\Theta CSL\ (\sum)| \leq 5°$. The Atex software (version 5.08) was used to calculate boundary misorientations and compare them to the theoretical CSL values.

The densification behavior of the LPBF-fabricated specimens was evaluated using EBSD band contrast (BC) mapping. Band contrast, which quantifies the quality of the diffraction pattern at each measurement point, serves as an effective proxy for identifying volumetric defects. In the generated maps, regions of high crystalline perfection appear bright, while features such as grain boundaries, lattice distortion, and voids exhibit significantly lower contrast intensities.

Defects such as gas porosity and lack-of-fusion voids were identified as non-indexed regions characterized by negligible BC and a Confidence Index (CI) approaching zero. By filtering out HAGBs (which also exhibit zero or low BC values) based on the minimum grain size threshold defined in the methodology, the remaining zero-solution regions could be attributed to true voids rather than boundary artefacts. These areas were subsequently quantified to estimate the residual porosity, enabling a correlation between chemical composition and defect density.

2.4. Mechanical Property Characterization

Vickers microhardness $HV_{0.3}$ measurements were performed on the polished cross-sections of the as-built samples using a Future-Tech FM-ARS microhardness tester. A load of 300 g (2.94 N) was applied with a dwell time of 15 s. To ensure statistical reliability, a minimum of 10 indentations were recorded for each sample composition.

Uniaxial tensile tests were performed using a universal testing machine (Zwick Z100, ZwickRoell, Ulm, Germany) equipped with a 100 kN load cell. The tests were conducted at room temperature with a constant crosshead speed of 2 mm/min in accordance with the ASTM E8 standard [27].

3. Results

3.1. Porosity Analysis

Figure 1 presents the BC maps of the three samples investigated in this study. The reference 2507 SDSS sample exhibits a low porosity of approximately 0.8% (area fraction), indicating nearly full densification (Figure 1a). A comparable level of densification is maintained upon nickel addition. Specifically, the 2507 + 3 wt.% Ni and 2507 + 6 wt.% Ni alloys show porosity levels of approximately 0.8% and 0.5%, respectively (Figure 1b,c). These results demonstrate that nickel addition does not adversely affect densification under the

applied LPBF processing conditions. Furthermore, the defect morphology remained consistent across all conditions, characterized primarily by small, spherical gas pores, as well as a lack of fusion defects typical of the LPBF process (see Supplementary Figure S1) [28–30]. It is important to note that while the 2507 + 3% Ni sample exhibited some surface scratches, these preparation artifacts were systematically excluded from the image analysis to ensure accurate porosity quantification.

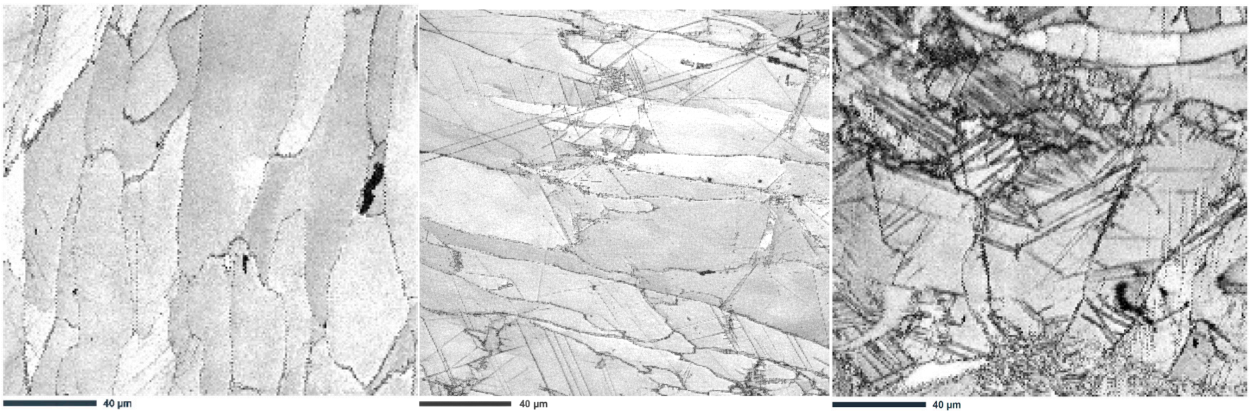

(**a**) (**b**) (**c**)

Figure 1. EBSD band contrast (BC) maps illustrate the residual porosity of the LPBF-fabricated super duplex stainless-steel samples: (**a**) Base 2507, (**b**) 2507 + 3% Ni, and (**c**) 2507 + 6% Ni. The high intensity of the band contrast pattern across all samples indicates a high degree of densification. Residual porosity appears as dark, non-indexed regions, primarily characterized by small, spherical gas pores. Note that the linear features visible in (**b**) are surface scratches resulting from metallographic preparation and were systematically excluded from the quantitative porosity analysis.

3.2. Microstructure Evolution

The evolution of phase constituents within the as-LPBF microstructures was assessed using EBSD phase mapping (Figure 2). As shown, the reference 2507 SDSS sample exhibits a ferrite phase fraction of 98.5% (Figure 2a). A small amount of austenite (1.5 wt.%) appears mainly as a thin film at ferrite grain boundaries. This ferrite-dominated morphology is consistent with numerous reports on LPBF-processed duplex stainless steels, which also reveal a largely ferritic microstructure in the as-built condition [31–34]. It is worth noting that XRD analysis of the same as-printed sample indicated a ferrite fraction of approximately 93% [35]. The discrepancy between the EBSD measurement (98.5% ferrite) and the XRD result (93% ferrite) is attributed to the specific physical limitations of each method. XRD analysis provides a bulk volumetric assessment but is sensitive to the strong crystallographic texture, which can skew peak intensities used for phase quantification. Conversely, EBSD offers precise spatial resolution but may underestimate the austenite fraction if fine intergranular austenite falls below the step-size resolution or exhibit poor band contrast due to high residual strain. Thus, while EBSD accurately depicts the morphology of the resolvable grains, the XRD value likely captures the total phase content, including sub-micron features, more effectively.

Addition of 3% Ni has a minimal effect on the phase balance of the LPBF-fabricated 2507 SDSS, as shown in Figure 2b. Microstructural analysis shows that the solidification mode remains in the primary ferrite regime. Had the solidification mode shifted to primary austenite, the microstructure would typically exhibit large columnar grains with low twin density, as observed in high-Ni austenitic steels [36]. Instead, the observed ferritic matrix with intragranular austenite laths (8.56 wt.%) indicates that Ni did not alter the solidification pathway but rather increased the thermodynamic driving force for the solid-state ferrite to

austenite transformation upon cooling, allowing a larger volume fraction of austenite to nucleate and grow within the ferrite grains.

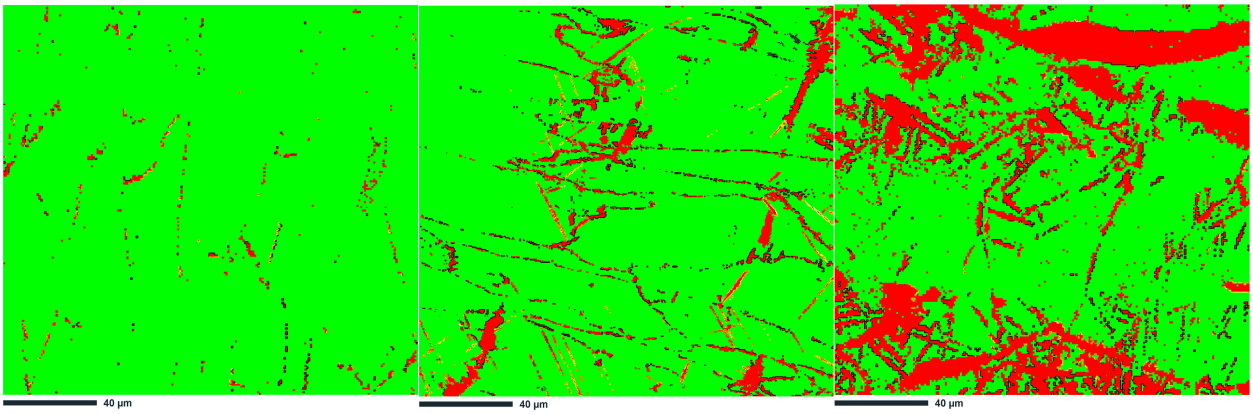

(**a**) (**b**) (**c**)

Figure 2. Results of EBSD phase analysis of the LPBF-fabricated 2507 super duplex stainless-steel samples: (**a**) Base 2507, (**b**) 2507 + 3% Ni, and (**c**) 2507 + 6% Ni. Phases are labeled as follows: green—δ-ferrite; red—γ-austenite. Black lines indicate grain boundaries satisfying the Kurdjumov–Sachs orientation relationship, while yellow lines denote those corresponding to the Nishiyama–Wassermann relationship.

In the sample fabricated from powder feedstock over-alloyed with 6 wt.% Ni (Figure 2c), the austenite fraction is approximately 31.1 wt.%**.** The phase map reveals a pronounced fraction of intragranular γ-austenite within the δ-ferrite grains. This indicates that Ni enrichment enhances γ nucleation not only at δ/δ grain boundaries but also within ferrite grain interiors. Consequently, the resulting microstructure is characterized by coarse δ-ferrite grains containing fine, lath-like austenite. Such morphology indicates that the repeated thermal cycling inherent to the LPBF process may promote the δ→γ solid-state transformation under conditions of increased austenite-stabilizing element content.

To understand the transformation mechanism, the crystallographic orientation relationships between the ferrite matrix and austenite were analyzed. The EBSD orientation data demonstrate strong interphase coherency, frequently satisfying the Kurdjumov–Sachs (K–S) orientation relationship $[111]_{\text{ferrite}} \,||\, [110]_{\text{austenite}}$. In the sample fabricated from powder feedstock over-alloyed with 6 wt.% Ni, 81.98% of all measured δ–γ boundaries exhibit K–S alignment, whereas only 18.02% corresponded to the Nishiyama–Wassermann (N–W) relationship. When expressed as boundary length fractions, K–S interfaces account for 34.9% of all δ–γ interfaces and 23.6% of the total boundary network. The dominance of K–S interfaces suggests that the transformation minimizes interfacial energy through rational atomic matching, in accordance with interpretations proposed for massive-like transformations [35]. As proposed by Haghdadi et al. [37], this orientation relationship is maintained during rapid growth through the formation of twinning events, which allow the austenite to reorient and maintain coherency with the ferrite matrix. The preservation of these specific orientation relationships supports the notion that the δ→γ transformation is stimulated by the repetitive reheating intrinsic to LPBF, analogous to the reheating of quenched duplex steels, where K–S and N–W relationships are frequently reported [38,39].

In comparison, the sample fabricated from powder feedstock over-alloyed with 3 wt.% Ni demonstrated a broader variant distribution. Here, 57.6% of δ–γ boundaries satisfied K–S alignment, whereas 42.4% corresponded to N–W matching. On a boundary-length basis, K–S and N–W accounted for 36.9% and 27.1% of δ–γ interfaces (and 27.7% versus 20.4% of the total boundary network), respectively. This more balanced variant population

implies weaker energetic constraints during nucleation, resulting in an environment where multiple crystallographic pathways operate concurrently.

Despite the prevalence of rational matching, quantitative analysis confirms that interphase coherency is not universal. A fraction of δ–γ interfaces deviate from ideal K–S/N–W alignment, indicating the coexistence of rational and irrational orientation relationships. This deviation can be attributed to the competitive formation of high-temperature austenite, which typically preserves K–S continuity, and low-temperature austenite formed under rapid cooling, which incorporates substantial stored strain. As proposed by Liu et al. [40], this accumulated strain energy, combined with the thermal activation from the intrinsic heat treatment of subsequent layers, can drive a partial recrystallization of the austenite. This recrystallization modifies local crystallographic orientation and disrupts initial coherency with the parent δ matrix, ultimately giving rise to the observed population of irrational interfaces.

The histograms of misorientation angle distributions of the analyzed specimens are shown in Figure 3, revealing a change in misorientation angle distribution with an increasing Ni content. In the reference DSS 2507 alloy (Figure 3a), the distribution exhibits a distinct bimodal character, consisting of a population of low-angle grain boundaries (LAGBs, <5°) and a relevant high-angle peak at ~45°, reaching a number fraction of approximately 20%. The relatively high fraction of LAGBs is indicative of the extensive sub-grain and dislocation structures formed during rapid solidification, which is inherent to LPBF processing.

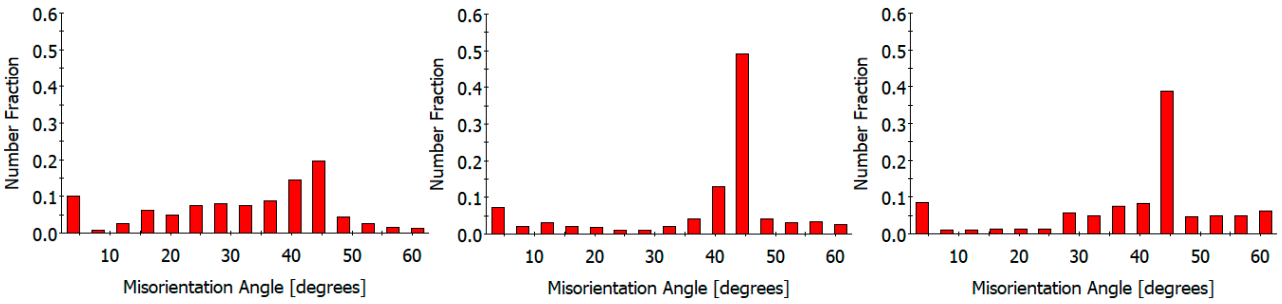

Figure 3. Histograms of misorientation angle distributions for LPBF-fabricated 2507 super duplex stainless steel: (**a**–**c**) histograms corresponding to the base alloy, 3 wt.% Ni, and 6 wt.% Ni conditions, respectively. The histograms illustrate the relative fractions of low-angle and high-angle boundaries and their evolution with nickel addition.

Upon the addition of 3 wt.% Ni to the powder feedstock (Figure 3b), the misorientation profile broadens considerably. The intensity of the 45° peak decreases to roughly 0.20, accompanied by an increased presence of HAGBs between 15° and 40°. This redistribution suggests that intermediate nickel enrichment perturbs solidification dynamics and/or phase transformation pathways, promoting a more heterogeneous interphase crystallographic alignment.

Conversely, the alloy over-alloyed with 6 wt.% Ni (Figure 3c) exhibits a substantial sharpening of the texture. The random HAGBs are significantly diminished and the ~45° peak intensifies, reaching nearly 0.50 in number fraction. This specific misorientation is consistent with the Kurdjumov–Sachs (K–S) orientation relationship typically observed between ferrite and austenite (~42.6–46°).

Following the analysis of the misorientation distributions for both γ and δ phases (Figure 3), a separate examination was conducted for the austenite phase alone to isolate the evolution of boundary character within the γ phase (Figure 4a–c). In the base alloy (Figure 4a), the austenite misorientation angle distribution profile is relatively broad, with

a dominant peak at ~45°, consistent with the misorientation signature expected for δ→γ transformation products formed under LPBF cooling conditions.

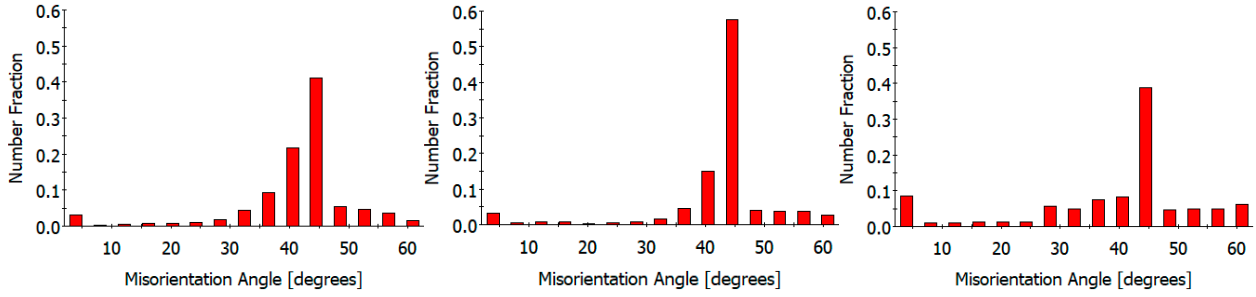

Figure 4. Histograms of misorientation angle distributions for the austenite phase in LPBF-fabricated 2507 super duplex stainless steel: (**a**–**c**) histograms corresponding to the base alloy, 3 wt.% Ni, and 6 wt.% Ni conditions, respectively.

With 3 wt.% Ni (Figure 4b), this peak becomes more prominent and the distribution narrows, indicating that a greater proportion of the austenite-ferrite interfaces adopt the K-S orientation relationship.

A noticeable change in the misorientation angle distribution is observed for the 6 wt.% Ni alloy (Figure 4c). The peak near ~45° becomes less dominant compared to the 3 wt.% Ni condition, and a secondary feature appears around ~60°. The increasing presence of ~60° misorientations suggests that the microstructure progressively incorporates twin-related, ∑3 boundaries as the nickel concentration rises.

To visualize the spatial distribution of special grain boundaries and their correlation with the evolving phase constituents, EBSD maps with superimposed CSL boundaries were generated (Figure 5). In the reference 2507 sample (Figure 5a), the sparse grain-boundary austenite exhibits a negligible fraction of CSL interfaces.

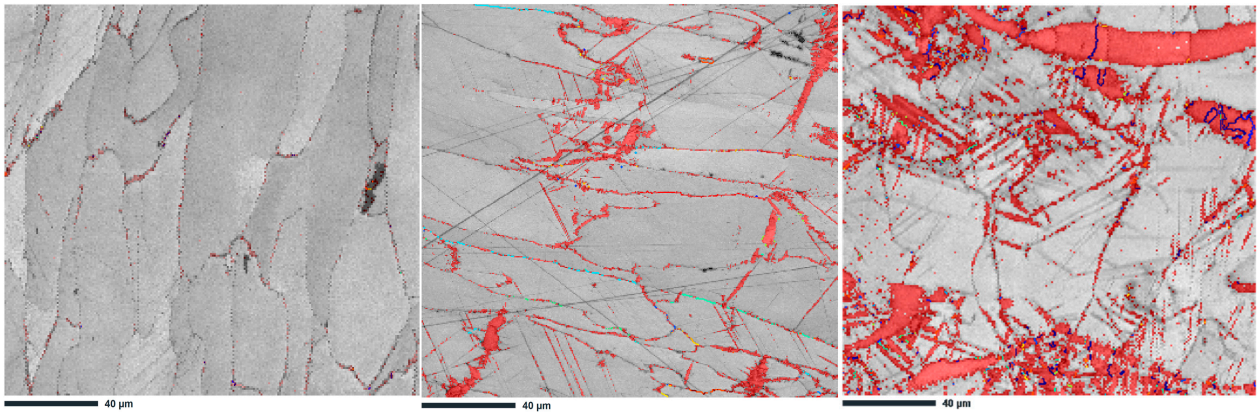

Figure 5. EBSD phase map of the LPBF-fabricated 2507 super duplex stainless steel with superimposed CSL boundaries. (**a**) Base 2507, (**b**) 2507 + 3% Ni, and (**c**) 2507 + 6% Ni. Austenite regions are shown in red, and ferrite in gray, while CSL boundaries are highlighted in accordance with a color coding in Figure 6 to illustrate their spatial distribution within the microstructure. The overlay reveals how CSL-type boundaries are incorporated into the transformed austenite network and their interaction with ferrite regions.

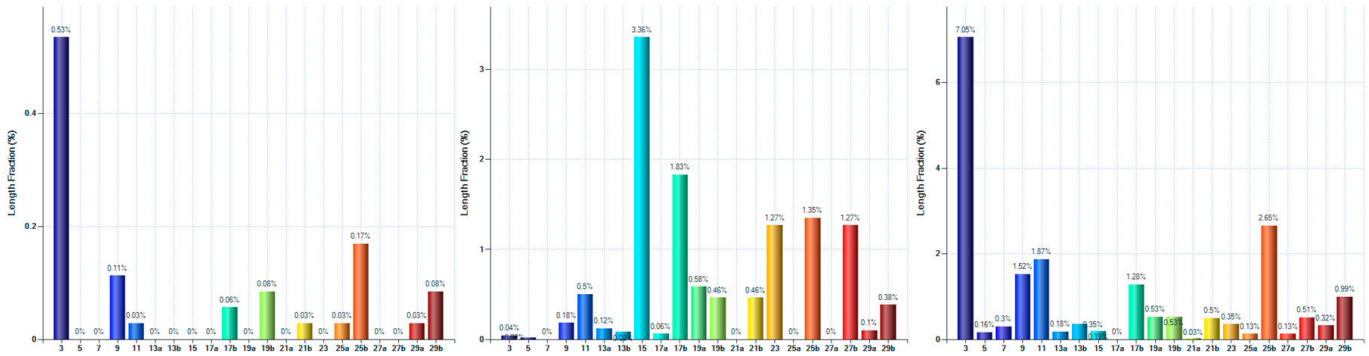

(**a**) (**b**) (**c**)

Figure 6. CSL boundary statistics derived from EBSD analysis of the LPBF-fabricated 2507 super duplex stainless steel. The histograms display the relative frequency of ∑3 and higher-order CSL boundaries within the austenite phase for the (**a**) base, (**b**) 3 wt.% Ni, and (**c**) 6 wt.% Ni conditions. The distributions highlight how nickel addition modifies the proportion of twin-related interfaces and reflect the progressive evolution of the austenite boundary network.

A noticeable change in the GBCD is observed with nickel addition. In the 6 wt.% Ni alloy (Figure 5c), the austenite regions (red) are significantly expanded and internally segmented by a network of CSL boundaries (blue). These special boundaries are not confined to interphase regions but extend across the interiors of austenite grains, thereby interrupting the continuity of the random high-angle grain boundary network. This observation indicates that austenite formed through the massive-like $\delta \rightarrow \gamma$ transformation during the intrinsic thermal cycling of the LPBF process retains the ability to form twin-related CSL boundaries, despite the high cooling rates of LPBF.

The quantitative evolution of the grain boundary character distribution (GBCD) is presented in Figure 6. For the reference alloy and the 3 wt.% Ni variants (Figure 6a,b), the histograms reveal a negligible population of ∑3 boundaries, with length fractions remaining close to the background level across the full CSL spectrum. The boundary population in these samples (Figure 4a,b) is dominated by random high-angle grain boundaries, which is consistent with the limited austenite fraction revealed by EBSD analysis. In contrast, the addition of 6 wt.% Ni leads to a more pronounced modification in the GBCD (Figure 6c). A sharp increase in the length fraction of ∑3 boundaries is observed, such that they dominate the austenite grain boundary network. This is accompanied by elevated fractions of higher-order Σ boundaries (e.g., ∑9 and ∑27), which is consistent with multiple twinning events and suggests a synergy of twinning mechanisms driven by the complex thermal history of LPBF. We propose that the primary population of ∑3 boundaries originates as transformation growth twins inherent to the massive-like transformation mode [41]. As detailed by Haghdadi et al. [37], these twins form to facilitate variant selection, allowing the austenite to maintain a low-energy K-S relationship with the parent ferrite during rapid interface migration. Subsequently, the intrinsic heat treatment induced by the deposition of successive layers likely activates twin regeneration mechanisms [16,42,43]. During these reheating cycles, the interaction of existing ∑3 boundaries facilitates the generation of higher-order variants (∑9, ∑27), thereby modifying the grain boundary network.

3.3. Mechanical Properties

The base 2507 SDSS exhibited a uniform Vickers microhardness of 369.0 ± 1.5 HV0.3. In the Ni-modified samples, the average hardness remained comparable for the 3 wt.% Ni sample (359.7 HV0.3) and increased slightly for the 6 wt.% Ni sample (397.7 HV0.3). This increase may be associated with a higher dislocation density [44], although a detailed

substructural analysis is beyond the scope of this study. Notably, the Ni-modified samples exhibited a significant increase in the standard deviation of microhardness values (±46.1 and ±37.2 HV0.3). This substantial scatter correlates with the observed microstructural heterogeneity of the alloy, indicating that the indentation response is spatially dependent. The variability suggests that the indenters are interacting with distinct local phase constituents, effectively capturing the intrinsic softening associated with the stabilized austenite regions within the harder ferritic matrix.

Complementing the microhardness results, tensile testing revealed a distinct trade-off between strength and ductility induced by the nickel additions. The reference 2507 SDSS displayed characteristic high strength but low ductility, recording a yield strength of 1310 ± 17.3 MPa, ultimate tensile strength (UTS) of 1392.5 ± 4.3 MPa, and elongation of 2.4 ± 0.5%. In the sample fabricated from powder feedstock over-alloyed with 3 wt.% Ni elongation increased to 6.8 ± 1.7%, while the yield strength and UTS decreased to 1094.6 ± 14.8 MPa and 1324.3 ± 22.0 MPa, respectively. This enhancement in ductility at the expense of strength was most pronounced in the sample fabricated form modified powder feedstock over-alloyed with 6 wt.% Ni, which achieved the highest ductility with an elongation of 17.0 ± 1.0%—a nearly seven-fold increase compared to the base alloy—accompanied by a reduction in yield strength to 809.9 ± 11.1 MPa and UTS to 976.6 ± 9.4 MPa. This significant increase in ductility is attributed not only to the higher volume fraction of the ductile austenite phase but also to the increased population of CSL boundaries. These special boundaries (particularly ∑3 twins) enhance the grain boundary network's resistance to crack propagation and facilitate better strain accommodation during plastic deformation [45].

4. Conclusions

This study investigated the feasibility of GBE in LPBF SDSS 2507 through the addition of nickel. After analyzing the microstructural evolution, phase balance, and crystallographic orientation relationships, the following conclusions can be drawn:

1. The addition of elemental nickel powder (up to 6 wt.%) to the SDSS 2507 feedstock did not compromise the densification behavior of the LPBF-processed material. All samples achieved a relative density exceeding 99.2%, with defects primarily limited to small, spherical gas pores typical of the process.
2. Nickel acted as a potent austenite stabilizer, effectively counteracting the rapid cooling rates of LPBF that favor ferrite retention. The austenite weight fraction increased from a negligible 1.5% in the base alloy to approximately 31.1% in the sample modified with 6 wt.% Ni.
3. The phase transformation in the high-nickel samples was governed by rational orientation relationships. The 6 wt.% Ni sample exhibited a strong preference for the Kurdjumov–Sachs (K–S) relationship, which accounted for nearly 82% of the δ–γ interfaces. This suggests that the stabilization of austenite promotes a transformation pathway that minimizes interfacial energy through coherent atomic matching.
4. Quantitative analysis of the GBCD indicated that the length fraction of ∑3 twin boundaries remained negligible (<0.6%) in both the base 2507 and 3 wt.% Ni samples. Conversely, increasing the nickel content to 6 wt.% resulted in a significant increase of ∑3 boundary fraction rising sharply to 7.05% within the austenite phase.

While this study confirms that nickel modification effectively restores phase balance and promotes GBE in as-built LPBF 2507, several critical avenues for future research remain to fully validate this approach for industrial application. First, although the microstructural prerequisites for enhanced durability—specifically the high fraction of ∑3 twin boundaries—have been established, their direct impact on corrosion performance requires

experimental verification. Future investigations will utilize electrochemical impedance spectroscopy and critical pitting temperature testing to quantify whether this in situ GBCD optimization translates to superior resistance against intergranular corrosion and stress corrosion cracking in aggressive chloride environments compared to conventionally heat-treated counterparts. Second, to resolve the fundamental metallurgical paradox regarding twin formation in high-SFE austenite, high-resolution Transmission Electron Microscopy studies are necessary. These analyses will aim to visualize the atomic-scale interactions between partial dislocations and stacking faults, providing definitive evidence of the twinning mechanisms active during the intrinsic thermal cycling of the LPBF process. Finally, acknowledging the economic implications of using high-nickel feedstock, future work will expand beyond fundamental material science to assess industrial viability. This will include a comprehensive evaluation of the modified alloy's weldability and machinability, alongside a cost–benefit analysis comparing the expense of compositional modification against the operational costs of traditional post-process solution annealing.

Supplementary Materials: The following supporting information can be downloaded at: https://www.mdpi.com/article/10.3390/sym18010198/s1, Figure S1: Light microscopy images of the LPBF-fabricated 2507 super duplex stainless-steel samples: (a) Base 2507, (b) 2507 + 3% Ni, and (c) 2507 + 6% Ni.; Figure S2: EDS elemental mapping of the 2507 + 6 wt.% Ni sample. The maps reveal a uniform distribution of Nickel and other alloying elements throughout the matrix, confirming the chemical homogeneity of the printed material. Figure S3: Pointwise EDS elemental analysis of the LPBF-fabricated 2507 SDSS modified with 6 wt.% Ni. (a) SEM micrograph indicating the specific point locations selected for analysis; (b) corresponding quantitative chemical composition data showing the distribution of major alloying elements.

Author Contributions: Conceptualization, P.S.; methodology, P.S.; investigation, P.S., B.A., M.K. (Michal Kotoul) and M.D.; formal analysis, P.S.; data curation, P.S.; writing—original draft preparation, P.S.; writing—review and editing, P.S., M.K. (Mariusz Król), M.K. (Michal Kotoul) and Z.B.; visualization, P.S.; supervision, Z.B.; resources, M.K. (Mariusz Król) and M.K. (Michal Kotoul); project administration, P.S.; funding acquisition, Z.B., M.K. (Mariusz Król) and P.S. All authors have read and agreed to the published version of the manuscript.

Funding: This research was funded by the National Science Centre, Poland, under decision number 2024/53/B/ST8/03574. Additionally, ZB and MK gratefully acknowledge support from the European Union Structural Funds project 'Innovative and additive technologies for sustainable energy industry' (registration No. CZ.02.01.01/00/23_021/0010117).

Data Availability Statement: The original contributions and microstructure images presented in this study are included in this article/Supplementary Materials. The raw EBSD datasets supporting these findings are openly available in the Zenodo repository at: https://doi.org/10.5281/zenodo.18198956.

Acknowledgments: M.Ko. supervised P.S.'s work within the framework of the Visegrad Fund International Scholarship Grant received by Przemysław Snopiński for the period from September 2025 to June 2026. B.A. received financial support from the Silesian University of Technology, grant number BKM 661/RMT-1/2025 (10/010/BKM_25/1247).

Conflicts of Interest: The authors declare no conflicts of interest.

References

1. Muñoz, J.A.; Chand, M.; Signorelli, J.W.; Calvo, J.; Cabrera, J.M. Strengthening of Duplex Stainless Steel Processed by Equal Channel Angular Pressing (ECAP). *Int. J. Adv. Manuf. Technol.* **2022**, *123*, 2261–2278. [CrossRef]
2. Köhler, M.L.; Kunz, J.; Herzog, S.; Kaletsch, A.; Broeckmann, C. Microstructure Analysis of Novel LPBF-Processed Duplex Stainless Steels Correlated to Their Mechanical and Corrosion Properties. *Mater. Sci. Eng. A* **2021**, *801*, 140432. [CrossRef]
3. Liljas, M.; Johansson, P.; Liu, H.-P.; Olsson, C.-O.A. Development of a Lean Duplex Stainless Steel. *Steel Res. Int.* **2008**, *79*, 466–473. [CrossRef]

4. Cui, C.; Becker, L.; Gärtner, E.; Boes, J.; Lentz, J.; Uhlenwinkel, V.; Steinbacher, M.; Weber, S.; Fechte-Heinen, R. Laser Additive Manufacturing of Duplex Stainless Steel via Powder Mixture. *J. Manuf. Mater. Process.* **2022**, *6*, 72. [CrossRef]
5. Papula, S.; Song, M.; Pateras, A.; Chen, X.-B.; Brandt, M.; Easton, M.; Yagodzinskyy, Y.; Virkkunen, I.; Hänninen, H. Selective Laser Melting of Duplex Stainless Steel 2205: Effect of Post-Processing Heat Treatment on Microstructure, Mechanical Properties, and Corrosion Resistance. *Materials* **2019**, *12*, 2468. [CrossRef]
6. Zheng, C.; Zhang, C.; Wang, X.Y.; Gu, J. Investigation of Mechanical and Corrosion Behavior of Laser Hybrid Weld Joint of 2205 Duplex Stainless Steel. *Anti-Corros. Methods Mater.* **2021**, *68*, 357–364. [CrossRef]
7. Baghdadchi, A.; Hosseini, V.A.; Hurtig, K.; Karlsson, L. Promoting Austenite Formation in Laser Welding of Duplex Stainless Steel—Impact of Shielding Gas and Laser Reheating. *Weld. World* **2020**, *65*, 499–511. [CrossRef]
8. Hu, Y.; Shi, Y.; Shen, X.; Wang, Z. Microstructure, Pitting Corrosion Resistance and Impact Toughness of Duplex Stainless Steel Underwater Dry Hyperbaric Flux-Cored Arc Welds. *Materials* **2017**, *10*, 1443. [CrossRef]
9. de Lima, M.S.F.; de Carvalho, S.M.; Teleginski, V.; Pariona, M.M. Mechanical and Corrosion Properties of a Duplex Steel Welded Using Micro-Arc or Laser. *Mater. Res.* **2015**, *18*, 723–731. [CrossRef]
10. Xiang, H.; Zhao, W.; Lu, Y. Effect of Solution Temperature on Microstructure and Mechanical Properties of Selective Laser Melted Fe-22Cr-5Ni-0.26N Duplex Stainless Steel. *J. Mater. Res. Technol.* **2022**, *19*, 1379–1389. [CrossRef]
11. Patra, S.; Agrawal, A.; Mandal, A.; Podder, A.S. Characteristics and Manufacturability of Duplex Stainless Steel: A Review. *Trans. Indian Inst. Met.* **2021**, *74*, 1089–1098. [CrossRef]
12. Francis, R.; Byrne, G. Duplex Stainless Steels—Alloys for the 21st Century. *Metals* **2021**, *11*, 836. [CrossRef]
13. Junior, E.J.C.; Gallego, J.; Settimi, A.G.; Gennari, C.; Zambon, A.; Ventrella, V.A. Influence of Nickel on the Microstructure, Mechanical Properties, and Corrosion Resistance of Laser-Welded Super-Duplex Stainless Steel. *J. Mater. Eng. Perform.* **2021**, *30*, 3024–3032. [CrossRef]
14. Li, H.; Thomas, S.; Hutchinson, C. Delivering Microstructural Complexity to Additively Manufactured Metals through Controlled Mesoscale Chemical Heterogeneity. *Acta Mater.* **2022**, *226*, 117637. [CrossRef]
15. Seita, M.; Gao, S. Broadening the Design Space of Engineering Materials through "Additive Grain Boundary Engineering". *J. Mater. Sci.* **2022**, *57*, 9530–9540. [CrossRef]
16. Randle, V. Twinning-Related Grain Boundary Engineering. *Acta Mater.* **2004**, *52*, 4067–4081. [CrossRef]
17. Dolzhenko, P.; Tikhonova, M.; Odnobokova, M.; Kaibyshev, R.; Belyakov, A. On Grain Boundary Engineering for a 316L Austenitic Stainless Steel. *Metals* **2022**, *12*, 2185. [CrossRef]
18. Sabzi, H.E.; Hernandez-Nava, E.; Li, X.-H.; Fu, H.; San-Martín, D.; Rivera-Díaz-del-Castillo, P.E.J. Strengthening Control in Laser Powder Bed Fusion of Austenitic Stainless Steels via Grain Boundary Engineering. *Mater. Des.* **2021**, *212*, 110246. [CrossRef]
19. Snopiński, P. Effects of KoBo-Processing and Subsequent Annealing Treatment on Grain Boundary Network and Texture Development in Laser Powder Bed Fusion (LPBF) AlSi10Mg Alloy. *Symmetry* **2024**, *16*, 122. [CrossRef]
20. Snopiński, P.; Matus, K. Characterisation of Microstructure and Special Grain Boundaries in LPBF AlSi10Mg Alloy Subjected to the KoBo Extrusion Process. *Symmetry* **2023**, *15*, 1634. [CrossRef]
21. Liu, B.; Ding, Y.; Xu, J.; Gao, Y.; Chu, C.; Hu, Y.; Chen, D. Grain Boundary Engineering Activated by Residual Stress during the Laser Powder Bed Fusion of Inconel 718 and the Electrochemical Corrosion Performance. *Mater. Charact.* **2023**, *204*, 113160. [CrossRef]
22. Guan, X.J.; Shi, F.; Ji, H.M.; Li, X.W. A Possibility to Synchronously Improve the High-Temperature Strength and Ductility in Face-Centered Cubic Metals through Grain Boundary Engineering. *Scr. Mater.* **2020**, *187*, 216–220. [CrossRef]
23. Andani, M.T.; Sundararaghavan, V.; Misra, A. Novel Approach to Grain Boundary Modification in Stainless and Duplex Steel L-PBF Components through In Situ Heat Treatment. *Crystals* **2023**, *13*, 1314. [CrossRef]
24. Wang, J.; Huang, H. Shockley Partial Dislocations to Twin: Another Formation Mechanism and Generic Driving Force. *Appl. Phys. Lett.* **2004**, *85*, 5983–5985. [CrossRef]
25. Liu, T.; Mukhopadhyay, S.; Li, C.-H.; Li, T.; Ren, Y.; Singh, P.; Devaraj, A. The Impact of Nickel Concentration and Stacking Fault Energy on Deformation Mechanisms in High-Purity Austenitic Fe-Cr-Ni Alloys. *Mater. Charact.* **2025**, *224*, 115046. [CrossRef]
26. Schramm, R.E.; Reed, R.P. Stacking Fault Energies of Seven Commercial Austenitic Stainless Steels. *Metall. Trans. A* **1975**, *6*, 1345–1351. [CrossRef]
27. *ASTM E8/E8M-24*; Standard Test Methods for Tension Testing of Metallic Materials. ASTM International: West Conshohocken, PA, USA, 2024.
28. Tang, M.; Pistorius, P.C.; Beuth, J.L. Prediction of Lack-of-Fusion Porosity for Powder Bed Fusion. *Addit. Manuf.* **2017**, *14*, 39–48. [CrossRef]
29. Ferro, P.; Fabrizi, A.; Berto, F.; Savio, G.; Meneghello, R.; Rosso, S. Defects as a Root Cause of Fatigue Weakening of Additively Manufactured AlSi10Mg Components. *Theor. Appl. Fract. Mech.* **2020**, *108*, 102611. [CrossRef]
30. Gao, Y.; Zhao, J.; Zhao, Y.; Wang, Z.; Song, H.; Gao, M. Effect of Processing Parameters on Solidification Defects Behavior of Laser Deposited AlSi10Mg Alloy. *Vacuum* **2019**, *167*, 471–478. [CrossRef]

31. Gargalis, L.; Karavias, L.; Graff, J.S.; Diplas, S.; Koumoulos, E.P.; Karaxi, E.K. A Comparative Investigation of Duplex and Super Duplex Stainless Steels Processed through Laser Powder Bed Fusion. *Metals* **2023**, *13*, 1897. [CrossRef]
32. He, C. Structure-Property Relationships in 2205 Duplex Stainless Steels via Laser Powder Bed Fusion 2025. Ph.D. Thesis, The University of New South Wales, Sydney, Australia, May 2025.
33. Gaudez, S.; Malamud, F.; Hearn, W.; Sumarli, S.; Strobl, M.; Van Petegem, S. Evolution of Texture and Residual Stresses in 2205 Duplex Stainless Steel during Laser Powder Bed Fusion. *Mater. Des.* **2025**, *251*, 113658. [CrossRef]
34. Haghdadi, N.; Ledermueller, C.; Chen, H.; Chen, Z.; Liu, Q.; Li, X.; Rohrer, G.; Liao, X.; Ringer, S.; Primig, S. Evolution of Microstructure and Mechanical Properties in 2205 Duplex Stainless Steels during Additive Manufacturing and Heat Treatment. *Mater. Sci. Eng. A* **2022**, *835*, 142695. [CrossRef]
35. Dagnaw, M.; Poudel, S.; Subedi, U.; Thapa, R.; Reimann, Ł.; Appiah, A.N.S.; Nuckowski, P.M.; Król, M.; Brytan, Z.; Moelans, N.; et al. Integrating Experiments and Phase Field Method through informatics for Tailored Corrosion Performance of Additively Steel Microstructures. *ChemRxiv* **2025**. [CrossRef]
36. Monier, L.; Veron, M.; Blandin, J.-J.; Martin, G.; Villaret, F.; Despres, A. Solidification Pathway and Ferrite-to-Austenite Massive Transformation in Austenitic Stainless Steels Processed by Laser Powder Bed Fusion. *Materialia* **2025**, *43*, 102505. [CrossRef]
37. Haghdadi, N.; Cizek, P.; Hodgson, P.D.; Tari, V.; Rohrer, G.S.; Beladi, H. Effect of Ferrite-to-Austenite Phase Transformation Path on the Interface Crystallographic Character Distributions in a Duplex Stainless Steel. *Acta Mater.* **2018**, *145*, 196–209. [CrossRef]
38. Karlsson, D.; Helander, T.; Bettini, E.; Hassila, C.-J.; Cedervall, J.; Sahlberg, M.; Harlin, P.; Jansson, U. Relationship between Microstructure, Mechanical Properties and Creep Behavior of a Cr-Rich Ferritic Stainless Steel Produced by Laser Powder Bed Fusion. *Alloys* **2022**, *1*, 263–276. [CrossRef]
39. Haghdadi, N.; Cizek, P.; Hodgson, P.D.; He, Y.; Sun, B.; Jonas, J.J.; Rohrer, G.S.; Beladi, H. New Insights into the Interface Characteristics of a Duplex Stainless Steel Subjected to Accelerated Ferrite-to-Austenite Transformation. *J. Mater. Sci.* **2020**, *55*, 5322–5339. [CrossRef]
40. Liu, G.L.; Yang, S.W.; Han, W.T.; Yan, P.P.; Wang, M.; Hu, Q.; Misra, R.D.K.; Shang, C.J.; Wan, F.R. The Simultaneous Occurrence of Kurdjumov-Sachs and Irrational Orientation Relationships between Delta-Ferrite and Austenite Phase in a 17Cr–5Ni Stainless Steel. *Mater. Sci. Eng. A* **2020**, *798*, 140122. [CrossRef]
41. Chen, J.; Ji, Y.; Lu, J.; Wang, W.; Zhou, L.; Qi, J.; Liu, P.; Chen, K. In-Situ Observation of Peritectic Solidification of Fe–C–Mn–Al Steel with High Manganese Under Different Cooling Rates. *Metall. Mater. Trans. B* **2025**, *56*, 4484–4494. [CrossRef]
42. Randle, V. Relationship between Coincidence Site Lattice, Boundary Plane Indices, and Boundary Energy in Nickel. *Mater. Sci. Technol.* **1999**, *15*, 246–252. [CrossRef]
43. Randle, V.; Hu, Y. The Role of Vicinal Σ3 Boundaries and Σ9 Boundaries in Grain Boundary Engineering. *J. Mater. Sci.* **2005**, *40*, 3243–3246. [CrossRef]
44. Nie, Y.J.; Yang, F.; Meng, L.X.; Wang, Y.Z.; Yin, L.; Shi, Q.X.; Ma, J.Y.; Liang, W.; Zheng, L.W. Dislocation Structures and Residual Stresses in Duplex Stainless Steel Fabricated by Laser Powder Bed Fusion with 430 and 316L Powders. *Mater. Sci. Eng. A* **2024**, *914*, 147127. [CrossRef]
45. Shen, T.; Feng, L.; Shao, Y.; Chen, Y.; Xia, X.; Chen, Y.; Zhao, W. Relationship between Phase Transformation and Corrosion Performance of 2205 Duplex Stainless Steel Fabricated by Laser Powder Bed Fusion. *Mater. Today Commun.* **2025**, *44*, 111919. [CrossRef]